AIAA JOURNAL
Vol. 46, No. 8, August 2008

Aeromechanics of Membrane Wings with Implications for Animal Flight

Arnold Song,* Xiaodong Tian,† Emily Israeli,‡ Ricardo Galvao,§ Kristin Bishop,¶ Sharon Swartz,** and Kenneth Breuer††
Brown University, Providence, Rhode Island 02912-9037

DOI: 10.2514/1.36694

Bats and other flying mammals are distinguished by thin, compliant membrane wings. In an effort to understand the dependence of aerodynamic performance on membrane compliancy, wind-tunnel tests of low-aspect-ratio, compliant wings were conducted for Reynolds numbers in the range of 0.7–2.0 × 10^5. The lift and drag coefficients were measured for wings of varying aspect ratio, compliancy, and prestrain values. In addition, the static and dynamic deformations of compliant membrane wings were measured using stereo photogrammetry. A theoretical model for membrane camber due to aerodynamic loading is presented, indicating that the appropriate nondimensional parameter describing the problem is a Weber number that compares the aerodynamic load to the membrane elasticity. Excellent agreement between the theory and experiments is found. Measurements of aerodynamic performance show that, in comparison with rigid wings, compliant wings have a higher lift slope, maximum lift coefficients, and a delayed stall to higher angles of attack. In addition, they exhibit a strong hysteresis both around a zero angle of attack as well as around the stall angle. Unsteady membrane motions were also measured, and it is observed that the membrane vibrates with a spatial structure that is closely related to the free eigenmodes of the membrane under tension and that the Strouhal number at which the membrane vibrates rises with the freestream velocity, coinciding with increasing multiples of the natural frequency of the membrane.

Nomenclature

A	=	cross-sectional area
$\mathbf{A}$	=	load cell voltage matrix
AR	=	aspect ratio
a	=	membrane wave speed
C	=	force balance calibration coefficients
$\mathbf{C}$	=	force balance calibration coefficient matrix
C_D	=	coefficient of drag
C_L	=	coefficient of lift
$C_{L_{\max}}$	=	maximum coefficient of lift
c	=	chord length
E	=	modulus of elasticity
F_n	=	chord-normal aerodynamic loading
$\mathbf{F}$	=	force vector
f_i	=	ith harmonic frequency
f_0	=	natural frequency
k_0	=	nondimensional frequency, $f_0 c/U$
Re	=	Reynolds number, $U_\infty c/\nu$
$\mathbf{S}$	=	diagonal singular matrix
T	=	membrane tension
T_0	=	pretension
t	=	membrane thickness
$\mathbf{U}$	=	left singular matrix
$\mathbf{V}$	=	right singular matrix
We	=	Weber number, $F_n/(Et)$
z	=	membrane chord-normal deflection
α	=	angle of attack
β	=	membrane contact angle
Δc	=	elongation length
Δp	=	pressure differential
ΔV	=	differential load cell voltage
ϵ	=	strain
ϵ_0	=	prestrain
ρ_m	=	mass per unit chord length
ρ	=	density of air

Presented as Paper 517 at the Aerospace Sciences Meeting, Reno, NV, 8–12 January 2008; received 16 January 2008; revision received 3 April 2008; accepted for publication 8 April 2008. Copyright © 2008 by the American Institute of Aeronautics and Astronautics, Inc. All rights reserved. Copies of this paper may be made for personal or internal use, on condition that the copier pay the $10.00 per-copy fee to the Copyright Clearance Center, Inc., 222 Rosewood Drive, Danvers, MA 01923; include the code 0001-1452/08 $10.00 in correspondence with the CCC.

*Graduate Research Assistant, Division of Engineering, Box D. Student Member AIAA.
†Assistant Engineer, Hazen and Sawyer, P.C., 498 Seventh Avenue, New York, NY 10018.
‡Graduate Research Assistant, Massachusetts Institute of Technology, Department of Aeronautics and Astronautics, 77 Massachusetts Avenue, Cambridge, MA 02139.
§Graduate Research Assistant, Massachusetts Institute of Technology, Department of Aeronautics and Astronautics, 77 Massachusetts Avenue, Cambridge, MA 02139.
¶Postdoctoral Fellow, University of California, Davis, Section of Evolution and Ecology, 1 Shields Avenue, Davis, CA 95616.
**Associate Professor, Department of Ecology and Evolutionary Biology, Box G-B2.
††Professor, Division of Engineering, Box D. Senior Member AIAA.

I. Introduction

WINGS composed of thin, compliant skin membranes are used in the natural world by several vertebrate species, perhaps most notably by flying and gliding mammals such as bats, flying squirrels, and marsupial gliders. These animals exhibit extraordinary flight capabilities with respect to maneuvering and agility that are not observed in other species of comparable size. Birds, which have been studied extensively, have relatively rigid wings with limited degrees of freedom, whereas insect flight, which occurs at much lower Reynolds numbers, can be characterized by the relatively simple articulated flapping motion of effectively rigid wings [1–3]. In contrast, bats have a high degree of articulation in the wing (the elbow, wrist, and finger joints) [4] and, more relevant to the current investigation, the wings of bats are composed of a highly anisotropic, compliant skin membrane (Fig. 1). These morphological features may be key in enabling bats to fly in such a remarkable fashion, yet little is known of the aerodynamic performance of vehicles with either highly articulated or compliant wings.

The study of the full complexity of mammalian flight is challenging but, nevertheless, considerable progress has been made recently. Most studies have focused on the animal's kinematic motion [5,6], their overall lift and drag characteristics [4,5,7], or the wake characteristics behind the animal [5,8,9]. However, a

Fig. 1 Examples of mammalian flight: a) *Cynopterus brachyotis*, and b) *Pteropus vampyrus* (photo courtesy of Richard Wainwright). The unique wing morphology of bats includes their skeletal structure and thin wing membranes. Note the large degree of camber in the wing. The unique aerodynamic properties of a compliant-membrane wing are believed to play a significant role in the high degree of maneuverability exhibited by bats in flight.

significant challenge in working with live animals (and something that is somewhat unfamiliar to the traditional aerodynamics community) is the requirement that the testing be accomplished in a safe and humane manner. Furthermore, it is difficult, if not impossible, to isolate the individual contribution of the various, interdependent aspects of an animal's morphology to its overall aerodynamic performance. One solution to these difficulties is to test, using more traditional engineering models, the key features of the biological system with the goal of understanding how each feature influences the aerodynamic performance of the complete animal. Features that might be isolated include the use of low-aspect-ratio (LAR) wings, the thin compliant membrane lifting surface, and the low-Reynolds-number regime ($Re < 2 \times 10^5$), at which many complex aerodynamic phenomena, such as the transition to turbulence and laminar separation, are present, yet extremely hard to predict [10,11].

Focusing on the effects of a low Reynolds number, Shyy et al. [12] used XFOIL, a two-dimensional analysis code, in a computational comparison of the low-Reynolds-number performance of several airfoils with a particular interest in the effects of airfoil thickness and camber. For Reynolds numbers based on chord length, $Re = 7.5 \times 10^4$–2.0×10^6, the well-known NACA 0012 and the CLARK-Y airfoil profiles served as verification of the XFOIL predictions and as the baseline for a comparison of the two airfoils optimized for low-Reynolds-number flight. The thinner and more cambered airfoils yielded higher lift-to-drag ratios and power efficiency, $C_L^{3/2}/C_D$, in the range of Reynolds numbers tested. This was particularly striking at the lowest Reynolds number, $Re = 7.5 \times 10^4$, at which the power efficiency of the designed airfoil was nearly 3 times that of the NACA 0012. Additionally, the authors examined the effects of the deformability of an airfoil. The top of a CLARK-Y airfoil was modeled in XFOIL as a flexible membrane that adopted an equilibrium shape for a particular angle of attack and freestream velocity. The authors concluded that the aerodynamic performance of the flexible and rigid airfoils were comparable. However, the airfoil with the flexible membrane top was less sensitive to oscillations in the freestream velocity.

Experimental studies by Pelletier and Mueller [13] and Torres and Mueller [14] reported on experiments with rigid, thin LAR airfoils of varying camber and planform shapes for $Re \approx 10^5$. These series of experiments characterized the effects of the aspect ratio and camber on lift, drag, and aerodynamic efficiencies and suggested that the wing tip vortices are responsible for the nonlinear regions of the lift curve for wings with aspect ratios of less than 1.25. These flow structures play a role similar to the tip vortices on a delta wing by providing vortex lift, particularly at high angles of attack, and contributing to an increase in maximum lift, $C_{L_{\max}}$, and a delay of stall at higher angles of attack, α.

There have been several previous studies of the aerodynamic characteristics of the changing shape of flexible yet inextensible airfoils, that is, sails, using thin-airfoil theory [15–17]. Thwaites [16] and Nielsen [15] found that the equilibrium shape is only a function of a tension parameter:

$$\lambda = 2\rho U_\infty^2 c/T \tag{1}$$

(using Thwaites's definition), and this idea will be extended to compliant wings in the present work. Subsequent studies have coupled numerical studies with experiments [18,19], showing good agreement between computations and experiments, although the computations require the separation point to be empirically determined. These studies, however, were limited to low angles of attack and low values of camber, which comprise only a small subset of conditions for compliant wings, particularly those observed in natural flyers. It is experimentally shown in this paper that compliant wings can reach camber values exceeding 10% of the chord length. Additionally, in vivo measurements of wing camber in bats flying in a wind tunnel [20] show that the camber of the skin membrane reaches similar values of near 10% during the downstroke, the portion of the wing beat during which a majority of the lift is produced.

More recently, several studies on the effects of compliance have reported on numerical techniques suitable for this highly coupled aeroelastic problem and on the improved performance of flexible membrane wings for micro air vehicles (MAVs) [10,12,21–24]. In this paper, we continue this exploration, although we step back to focus on a more canonical geometry, a simple rectangular membrane wing, presenting analytical and experimental results concerning both the static deflection and the unsteady behavior of LAR membrane wings. In particular, the experimental observations have been correlated with some relatively simple analytical predictions that help to explain how the aeroelastic coupling is mediated.

II. Analytical Considerations

Before describing the experiments, it is instructive to explore the predictions of a very simple theoretical model for a compliant wing subject to aerodynamic loading. The static aeroelastic deformation of a compliant membrane represents a balance between the aerodynamic forces generated by the airfoil shape and the tension in the membrane. A simple geometric model capturing this is presented in Fig. 2a. The model considers the two-dimensional projection of a membrane of thickness t and undeflected length c pinned between stationary leading and trailing edges. When subjected to aerodynamic loading, denoted by F_n in Fig. 2a, the membrane will deflect in the chord-normal direction, z, with contact angles β_{le} and β_{te}. Any aerodynamic forces generated by the leading- and trailing-edge structures are assumed to negligible in this model. For simplicity, we assume that the membrane adopts a parabolic shape, $z(x) = 4z_{\max}x(1-x)$. This is the exact solution for a membrane subjected to uniform loading and is a shape assumption that will be largely justified by our experimental results in Sec. IV.A. With this assumption, the membrane length is thus only a function of camber (defined as the maximum extension of the membrane, $z_{\max}$, which occurs in this model at midchord), and the contact angles at the leading and trailing edges, β_{le} and β_{te}, are equal: $\beta_{\text{le}} = \beta_{\text{te}} = \beta$.

For the membrane to be in static equilibrium, the membrane tension, T, per unit span must balance the aerodynamic forces, F_n,

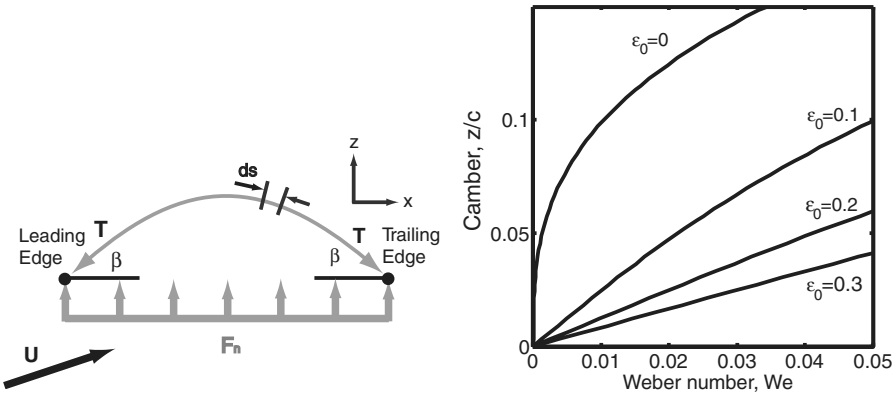

Fig. 2 Model for a compliant-membrane wing subject to aerodynamic loading: a) the membrane is modeled as a one-dimensional projection onto the span-normal plane subject to a uniform load, and b) camber as a function of the nondimensional aerodynamic loading characterized by the Weber number, $We = F_n/Et$. The camber increases rapidly at low aerodynamic loads, flattening as the load increases. Increased values of prestrain, ϵ_0, result in a more gradual deflection.

generated by the airfoil:

$$F_n = 2T\sin(\beta) = c\Delta p \tag{2}$$

where Δp represents an idealized uniform pressure difference between the lower and upper surfaces of the wing. Note that this pressure results from a combination of the dynamic pressure and the angle of attack. Increases in the membrane tension result from the elongation or stretching of the membrane when subjected to aerodynamic loading. Taking ds to be a differential element of membrane length, the elongation of the membrane, Δc, is given by

$$\Delta c = \int_{\text{le}}^{\text{te}} \mathrm{d}s - c \tag{3}$$

where the integral on the right-hand side of the equation is the arc length of the deflected membrane. For the simple model presented in this paper, the membrane is assumed to behave like a linearly elastic material with a modulus, E, which is independent of strain. In reality, both biological and man-made membranes are known to exhibit nonlinear J-shaped stress-strain behaviors for which E is strain dependent [25]. This behavior is ignored for the current analysis. Therefore, we express the membrane tension per unit width as only a function of the elongation length, Δc:

$$T = T_0 + Et\frac{\Delta c}{c} = T_0 + \frac{Et}{c}\left(\int_{\text{le}}^{\text{te}} \mathrm{d}s - c\right) \tag{4}$$

where the initial tension present in the undeflected membrane is denoted as T_0. Substituting this result into Eq. (2) and normalizing the aerodynamic loading by the product of the modulus and membrane thickness, we obtain an expression for the nondimensional aerodynamic loading, expressed as a Weber number, We:

$$\begin{aligned} We = F_n/Et = \Delta pc/Et &= 2[(T_0/Et) + (\Delta c/c)]\sin(\beta) \\ &= 2(\epsilon_0 + \epsilon)\sin(\beta) \end{aligned} \tag{5}$$

Using Eq. (5), we can determine the aerodynamic loading that can be supported by the membrane geometry with a prescribed camber value. For each value of the camber, $z_{\max}$, the elongation length, Δc, is calculated by integrating the contour of the camber line [Eq. (3)]. This elongation length determines the tension that, with the contact angle, β, determines the aerodynamic loading that can be supported by the membrane. Figure 2b presents the membrane camber as a function of the aerodynamic load for varying values of initial prestrain, $\epsilon_0 = T_0/Et$.

The camber-enhancing effect is most pronounced when there is no initial prestrain, that is, $\epsilon_0 = 0$, in which case we see that initially the membrane quickly adopts camber for very small aerodynamic loads. As the membrane deflects further, the camber dependence on the aerodynamic loading weakens and reaches an asymptotically linear dependence. The rapid initial rise in camber can be attributed to the fact that the undeflected membrane offers no resistance to any aerodynamic load (because a membrane has zero bending stiffness) and thus starts to camber immediately. At low loads, the small curvature of the membrane results in small values of both $\sin(\beta)$ and membrane elongation, Δc. Therefore, the chord-normal contribution of the tension is small and the membrane quickly "balloons" out. As the membrane deflects further from the chord line, this effect diminishes. This behavior is strongly dependent on the membrane prestrain, ϵ_0, which allows the membrane to support larger aerodynamic loads at lower values of camber. Therefore, the membrane camber shows a weaker dependence on the Weber number for increasing prestrain values, ϵ_0.

III. Experimental Procedure

The experiments were conducted in the Brown University low-speed wind tunnel. This is a closed-return facility with a constant-speed, variable-angle axial fan. The test cross section measures 61×58 cm (width by height) and has excellent flow quality, with a freestream turbulence measured to be less than 0.1% (0.1–10,000 Hz). The experiments were conducted at freestream velocities in the range of 8–21 m/s (measured by a pitot tube connected to a Baratron pressure transducer (MKS model 398HD), corresponding to Reynolds numbers based on the chord length of $\text{Re} = 7 \times 10^4$–$2 \times 10^5$.

A. Compliant Membrane Models

Compliant membrane half-wings were designed and manufactured for these experiments. The rectangular wings were composed of a compliant latex membrane held between two stainless steel posts mounted on an aluminum base plate. The steel posts defined the leading and trailing edges (Fig. 3). The membrane material was inserted through a slit aligned with the centerline of the post and then secured using spring steel clamps. With the clamps in place, the leading and trailing edges were approximately parabolic in shape with a maximum thickness of 3.7 mm. Although not sharp, the leading-edge curvature is nevertheless very small; thus, one expects that leading-edge separation will occur at small incidence angles. Using two sets of posts, with lengths of 6 and 9 cm and chord separations of 10 and 13 cm, we were able to fabricate wings with aspect ratios of $AR = 0.9$, 1.4, and 1.8.

Each half-wing was assembled by aligning the inner edges of the posts with reference lines on the membrane. The distance between the reference lines was equal to or shorter than the distance between the inner edges of the posts, resulting in an unprestrained or prestrained membrane, respectively. Thus, for the model with a prestrain value of 4%, the membrane was stretched so that it was 4% longer than its original relaxed state, that is, the distance between the inner edges of the posts. We should note that the assembly technique

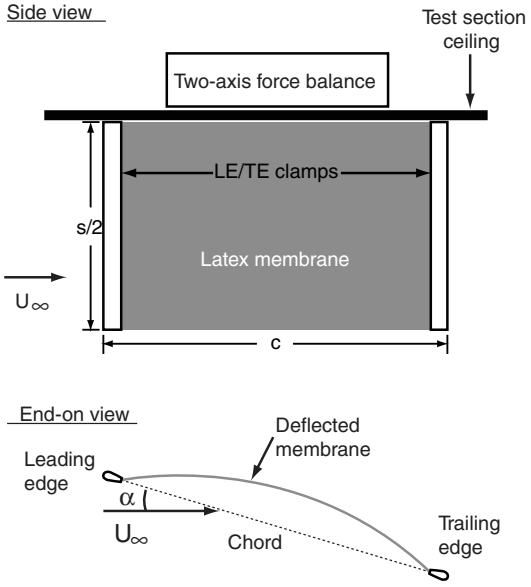

Fig. 3 Experimental setup. The compliant-membrane wings were composed of thin latex sheeting clamped at the leading and trailing edges. The edges at the root and tip were unconstrained and could deflect freely. The leading- and trailing-edge clamps were mounted to a plate that was attached to the sting arm of a two-axis force balance.

did not allow for precise control of the tension in the wing membrane. As a result, direct comparisons between wings of different membrane thicknesses are to be taken as qualitative, because the cambering behavior is a strong function of the membrane prestrain, ϵ_0; therefore, slight variations in ϵ_0 can have a marked effect on the cambering behavior, as discussed earlier.

B. Stereo Photogrammetry

A stereo photogrammetry system was developed to measure the instantaneous deflections of the membrane wings. Two high-speed complementary metal oxide semiconductor (CMOS) cameras (Photron 1024 PCI) were placed outside the wind-tunnel test section with an approximately 60–70 deg angle of separation between the respective optical axes (Fig. 3). The cameras have a resolution of 1024×1024 pixels, which, in conjunction with the imaging optics (Nikon 60 mm Micro Nikkor lenses), provided a spatial resolution of 0.20 mm per pixel. For this series of experiments, the unsteady motion of the membrane was recorded for 1.0 s at 1000 Hz (1000 frames) at each speed and angle of attack.

Each marker on the wing was tracked, and custom software, using direct linear transformation (DLT), was used to recover the coordinates of each marker location in the 3-D object space from two 2-D images at each time step [26]. A calibration cube consisting of a 3-D grid of markers was used to generate the calibration coefficients needed to reconstruct the coordinates in the object space via DLT. Using a test object that was moved in a controlled manner, we determined that the measurement uncertainty of the photogrammetry system was less than ± 35 μm for in-plane displacements and ± 40 μm for out-of-plane displacements, with the reference plane taken to be the chord line.

C. Lift and Drag Measurements

In a separate series of experiments, the wing was mounted on a gimballed, two-axis force balance to measure the lift and drag. The aerodynamic forces were determined from the differential output voltages of the load cells (OMEGA's LCKD Series subminiature compression load cells), ΔV_x and ΔV_z, placed at the ends of platforms corresponding to each measurement axis. The differential arrangement minimizes the common-mode noise due to vibration of the apparatus. The entire force balance assembly was mounted to a turntable that allowed adjustment of the angle of attack. As the angle of attack was varied, the orientation of the orthogonal platforms remained fixed with respect to the chord line of the wing.

At any given speed and angle of attack, the forces in the streamwise and spanwise directions may be determined from a linear combination of the four load cell voltages. Ideally, the output voltages of two load cells at the ends of each of the measurement platforms would correspond in an equal and opposite direction in response to a force. However, each load cell had a slightly different gain, and small misalignments between the platforms of the force balance were unavoidable. For this reason, the voltage differentials, ΔV_x and ΔV_z, of *both* load cell pairs were used to determine both F_x and F_z. The chordwise and chord-normal directions are denoted as x and z, respectively. The relationship between the output voltage of the load cells and forces can be expressed in matrix form:

$$\begin{bmatrix} C_{xx} & C_{xz} \\ C_{zx} & C_{zz} \end{bmatrix} \begin{bmatrix} \Delta V_x \\ \Delta V_z \end{bmatrix} = \begin{bmatrix} F_x \\ F_z \end{bmatrix} \tag{6}$$

The coefficient matrix, $\mathbf{C}$, was determined from a series of calibration measurements performed by applying static forces in both the chordwise and chord-normal directions. For each combination of applied loads, $[F_x; F_z]$, the differential load cell voltages, ΔV_x and ΔV_z, were measured. The calibration coefficients, C_{ij}, were then determined using a generalized linear regression of the overdetermined linear system:

$$\mathbf{A} \cdot \mathbf{C} = \mathbf{F} \tag{7}$$

where

$$\mathbf{A} = \begin{bmatrix} \Delta V_{x,1} & \Delta V_{z,1} & 0 & 0 \\ \vdots & \vdots & \vdots & \vdots \\ \Delta V_{x,N} & \Delta V_{z,N} & 0 & 0 \\ 0 & 0 & \Delta V_{x,1} & \Delta V_{z,1} \\ \vdots & \vdots & \vdots & \vdots \\ 0 & 0 & \Delta V_{x,N} & \Delta V_{z,N} \end{bmatrix}$$

$$\mathbf{C} = \begin{bmatrix} C_{xx} \\ C_{xz} \\ C_{zx} \\ C_{zz} \end{bmatrix}, \quad \text{and} \quad \mathbf{F} = \begin{bmatrix} F_{x,1} \\ \vdots \\ F_{x,N} \\ F_{z,1} \\ \vdots \\ F_{z,N} \end{bmatrix} \tag{8}$$

and the number of calibration measurements is denoted by N. We can decompose the matrix of measured voltages, $\mathbf{A}$, using singular value decomposition:

$$\mathbf{A} = \mathbf{U}\mathbf{S}\mathbf{V}^T \tag{9}$$

The dimension of the voltage matrix, $\mathbf{A}$, is $2N \times 4$. We define $\mathbf{S}$ to be a $2N \times 4$ diagonal matrix of singular values of the original matrix $\mathbf{A}$. $\mathbf{U}$ and $\mathbf{V}$ are then defined to be matrices of dimensions $2N \times 2N$ and 4×4 respectively, which have orthogonal columns, so that

$$\mathbf{U}^T\mathbf{U} = \mathbf{I} \tag{10}$$

and

$$\mathbf{V}^T\mathbf{V} = \mathbf{I} \tag{11}$$

The calibration coefficients, $\mathbf{C}$, are then solved for using

$$\mathbf{C} = \mathbf{A}^{-1}\mathbf{F} = \mathbf{V}\mathbf{S}^{-1}\mathbf{U}^T\mathbf{F} \tag{12}$$

Because the inverse of $\mathbf{S}$ is used to determine $\mathbf{C}$, artificially large coefficient values may result from the very small entries of $\mathbf{S}$, that is, singular values of negligible importance. We employed a threshold technique, in which the spuriously large values of $\mathbf{S}^{-1}$ were set to zero. A value was considered to be spuriously large if it was 50 times

higher than the minimum value of $\mathbf{S}^{-1}$. This calibration method was found to be accurate within 1.5% for loads larger than 1N and no worse than 5.0% for calibration loads less than 1N. The uncertainty in the force measurement is the most significant contributor to the overall uncertainty of the measurement apparatus. Uncertainties in the velocity, temperature, and ambient pressure measurements were all found to be less than 0.5%. Therefore, the uncertainties in the lift and drag coefficients for $Re = 1.4 \times 10^5$ were found to be no worse than 5% for values of C_L and C_D less than 0.5 and less than 1% for larger values of C_L and C_D.

IV. Results and Discussion

These experiments represent our first efforts in an ongoing investigation of compliant membrane wing aerodynamics in the context of mammalian flight. As a result, these initial experiments were deliberately broad in their scope in an attempt to identify as many of the critical features of compliant membranes salient to mammalian flight and MAV design. The results are organized as follows. In Sec. IV.A, the static deflection of the membrane is discussed. In Sec. IV.B, the lift and drag measurements are presented. Finally, in Sec. IV.C, the dynamic motion of the membrane is presented.

A. Static Membrane Deflection

For a nonzero value of the angle of attack, α, a compliant wing deflects and adopts a cambered shape. Stereo photogrammetry was used to reconstruct the three-dimensional geometry of the wing at several wind speeds and angles of attack. A typical time-averaged shape is shown in Fig. 4, and one sees several characteristic features, including the overall membrane deflection due to aerodynamic loading as well as enhanced deflection at both the root and wing tip. This last feature is discussed is more detail in the next section. As the load increases (either due to an increased air speed or angle of attack), the membrane stretches further, adopting higher camber that results in increased lift (according to thin-airfoil theory, the lift curve is shifted uniformly upward as the camber increases). Eventually, the membrane tension balances the aerodynamic load, resulting in the equilibrium wing shape illustrated in Fig. 4.

At these moderate angles of attack, the wing deflection was observed to be quite uniform along the span (with the exception of the root and tip regions) and well approximated by the parabolic assumption made in the theoretical model presented earlier. That model suggests that the maximum camber of a membrane wing is completely characterized by two parameters, the pretension, ϵ_0, and the Weber number,

$$We = \left(C_{L\frac{1}{2}}\rho U_\infty^2 c\right)/Et \tag{13}$$

where c and t are the chord length and membrane thickness, respectively. Figure 5 presents data from wings of two different latex thicknesses ($t = 0.1$ and 0.25 mm), fabricated with two values of prestrain ($\epsilon_0 = 0$ and 0.05), and tested over a wide range of freestream velocities ($U_\infty = 7$–16 m/s) and angles of attack ($\alpha = 4$–34 deg). With a few exceptions, we see that there is excellent agreement between the experimentally measured camber and the analytical predictions. To calculate the Weber number from the measurements, we have restricted ourselves to incidence angles below that at which stall was observed (see Sec. IV.B) and assumed that the lift force is proportional to the angle of attack: $C_L \propto \alpha$. For a two-dimensional airfoil, the constant of proportionality is 2π. However, for lower-aspect-ratio wings, the lift slope will be smaller, whereas the effect of compliancy will be to increase the lift slope. As a suitable compromise and for simplicity, we used a lift slope of 2π; indeed, we see (Fig. 5) that this choice matches the data extremely well, with the exception of a few outliers at relatively low values of the Weber number.

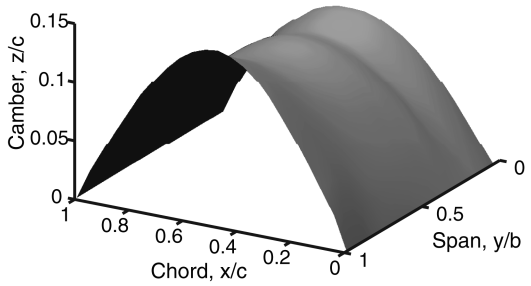

Fig. 4 Static deformation due to aerodynamic loading. The deformed membrane geometry is shown for $\alpha = 24$ deg and $Re_c = 1.4 \times 10^5$. The static surface geometry of the membrane is obtained from the time-averaged position of marker array. Note that the deflection of the membrane tip is greater than the root deflection due to the presence of a tip vortex.

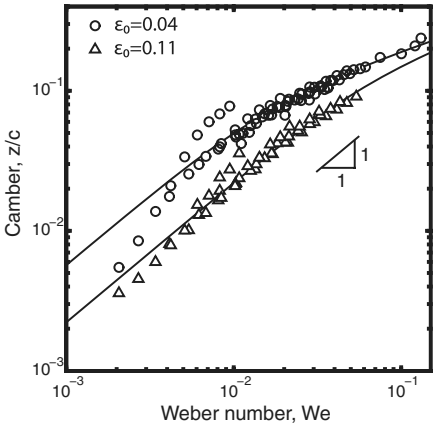

Fig. 5 Maximum camber as a function of aerodynamic loading. The maximum camber is plotted as a function of the Weber number, $We = \frac{1}{2}\rho U^2 c C_L/(Et)$, and compared with the theoretical model. Data presented are a composite assembled from several wings measured at 10 speeds ($U = 7$–16 m/s) and 12 angles of attack ($\alpha = 4$–34 deg). The wings represented two prestrains ($\epsilon_0 = 0.04$, 0.11) and two thickness ($t = 0.10$ and 0.25 mm). We only plot data for low angles of attack (i.e., prestall) for which the lift slope is approximately linear and the behavior is similar to that predicted by classical thin-airfoil theory. For such cases, the lift coefficient can be reasonably estimated to be $C_L = 2\pi\alpha$. There is excellent agreement between the experimentally observed camber behavior and the analytical model.

To compare experimental camber measurements with theory, the measurements were fit to the theoretical model by adjusting the value of the prestrain, ϵ_0. As noted earlier, we were not able to accurately measure the prestrain during wing fabrication. However, it was found that the best-fit data corresponded to prestrains of $\epsilon_0 = 0.04$ and 0.11, which were larger than the assumed values of 0 and 0.05, although the discrepancies are well within the bounds of our fabrication uncertainty. The data outliers at a low Weber number correspond to two regimes. The data points falling below the theoretical predictions are at the lowest speed tested. For these cases, we conclude that the lift force generated was lower than that predicted by our simple linear lift slope assumption and, consequently, the camber is lower, resulting in the poor agreement with the theory. The reason for this lower camber might be due to some nonideal bending stiffness at low aerodynamic loading that is not accounted for by the membrane theory. In contrast, the measurements that lie above the predicted values (both prestrains tested) are from measurements taken at high speeds but at low angles of attack. Here, the lift generated is likely higher than what would be predicted by the linear lift slope assumption, a conjecture that is strongly supported by the lift force measurements at high speeds (discussed in the next section).

A key component of the favorable lift characteristics of a low-aspect-ratio wing is the influence of the tip vortices over a greater portion of the wing. These tip vortices generate low-pressure regions over a significant portion of the wing, a phenomenon distinct from wings with larger aspect ratios for which these same tip vortices are confined to a smaller proportion of the lifting surface. Thus, for LAR

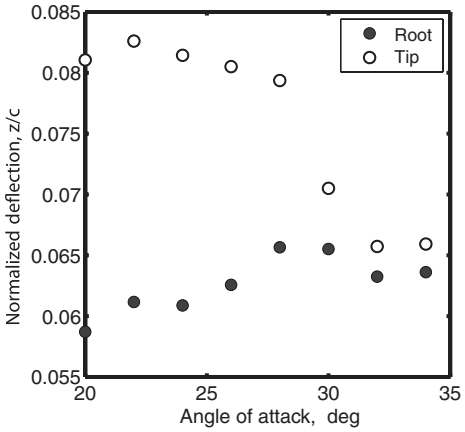

Fig. 6 Comparison of tip and root deflection. The influence of the tip vortex is particularly strong at low angles of attack, as indicated by the increased tip deflection relative to the root. However, the effect is diminished at stall.

wings, a greater fraction of the lift generated is due to tip vortex effects. In addition, the downwash from the tip vortices provides the chord-normal momentum needed for the flow to remain attached, thereby allowing a LAR wing to operate at higher angles of attack than would be possible for a wing with a higher aspect ratio at these moderate values of Reynolds number (Re $\approx$ 60–130 $\times$ 10^3) [27].

Although in the present experiments we cannot measure the pressure or the tip vortex structure, the shape of the membrane provides a window into the pressure distribution over the wing. In this half-span model, the tip and root were unconstrained (Fig. 4) and tended to deflect more than the bulk of the membrane. In addition, we observed a significant difference between the tip and root deflections (Fig. 6). These differences qualitatively indicate the strength of the tip vortex and its influence on the inboard portion of the wing. As the angle of attack rises, it is presumed that a strong vortex is generated at the leading edge due to the small leading-edge curvature. As the angle of attack is increased even further, this leading-edge vortex will likely become unstable and break away. This proposed bursting event, and the presence of separated flow on the upper surface of the wing, leads to an increase in the pressure over the inboard region of the wing and therefore weakens the tip vortex by decreasing the upper and lower surface pressure differential. The combination of the decrease in vortex strength and core size translates into a diminished contribution of vortex lift to the overall lift of the wing. We see this reflected in the relative deflections of the tip and root in Fig. 6. Before stall, the wing begins to experience a decrease in the lift slope corresponding to a change in the geometry. The inboard camber continues to increase, presumably due to the increasing lift. However, as the angle of attack is increased even further, the tip deflection begins to decrease or deflate, reflecting a weakening of the tip vortex. This deflation of the tip continues with the increasing angle of attack until a sharp drop in the tip deflection is observed. This tip deflation is strongly correlated with the drop in C_L and the lift slope at these higher angles of attack (discussed in the next section) and is presumed to be due to the bursting of the tip vortex at the onset of separation. These conjectures need to be confirmed with more detailed flow measurements, an experiment planned for the near future.

B. Lift and Drag Performance

An example of the typical aerodynamic performance of the compliant wing is seen in Fig. 7, which shows the lift and drag coefficients at different angles of attack for three different wings: a rigid wing (a stainless steel sheet) and compliant wings of two thickness ($t = 0.10$ and 0.25 mm). The rigid wing exhibits lift behavior typical of thin, low-aspect-ratio wings (Fig. 7a). The lift slope is nearly constant until a rather abrupt drop in lift, that is, stall, at higher angles of attack (between 20 and 30 deg). In contrast, the compliant wings exhibit several behaviors that are quite different. The less-compliant wing ($t = 0.25$ mm) has a higher lift slope and reaches a higher value of $C_{L_{\max}}$ than the rigid wing. Also, stall is delayed until much a higher range of angles of attack, between 30 and 40 deg. The most compliant model ($t = 0.10$ mm) continues this trend, reaching an even higher $C_{L_{\max}}$ and exhibiting a very soft stall behavior in the range of $\alpha = 30$–40 deg before lift is gracefully lost at angles in excess of 40 deg. The drag performance (Fig. 7b) also highlights the differences between the three models. The rigid wing drag performance can be characterized as a symmetric drag bucket with a slight hiccup at the onset of stall. Both compliant wings generate higher drag than the rigid wing over the entire range of angles tested, with the rise in drag becoming more pronounced as the compliance increases.

These behaviors are to be expected, given what we have observed about the wing deformation as the angle of attack increases. As the incidence angle rises, the camber increases; hence, the composite lift curve will have a lift slope that is higher than its rigid counterpart, because it is "sampling" the lift from a family of wings each with increasing camber. The higher lift is necessarily accompanied by higher (induced) drag, although it is also possible that the more-compliant wings also exhibit more drag due to losses associated with unsteady membrane motion.

Our theory predicts that a compliant wing will deform dramatically for low levels of aerodynamic loading, that is, small values of the Weber number, and that the rise in camber vs α slows as the aerodynamic load continues to increase (Fig. 5). This is

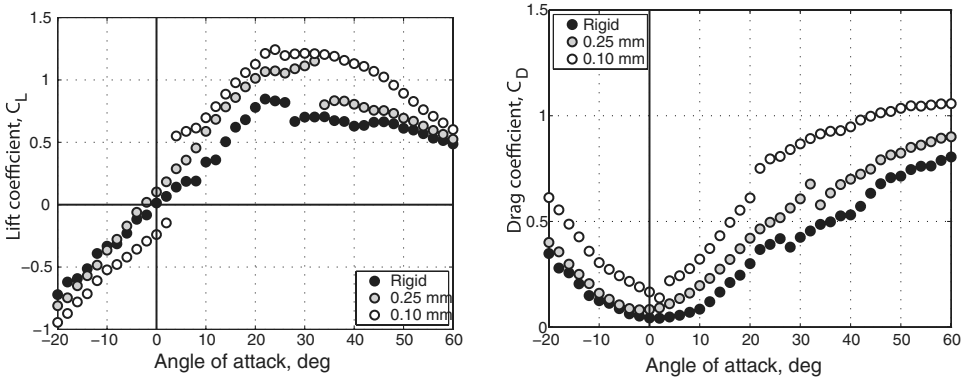

a) Lift perfromance **b) Drag perfromance**

Fig. 7 Aerodynamic performance of rigid vs compliant wings. The lift and drag coefficients of rigid and compliant wings of aspect ratio 1.4 are compared over a range of angles of attack. The compliant wing exhibits significant lift enhancement at low angles of attack and enhanced maximum lift. Both effects are due to the camber induced by the aerodynamic loading. The stall characteristic of the thinner and more-compliant wing is much less severe than the less-compliant-membrane wing and the rigid wing, due to automatic decambering at the onset of separation. The drag of the compliant wings is uniformly higher than that of their rigid counterpart. ($Re = 1.4 \times 10^5$)

confirmed by the rapid increase in C_L for the thinner latex membrane ($t = 0.10$ mm) and the lower value of the lift slope at higher angles of attack. The soft stall behavior may also be understood by recognizing that, as the laminar separation bubble begins to grow, the pressure on the upper surface rises, leading to an automatic decambering of the membrane (Fig. 6) and a backing away of the wing from the fully separated flow. This "aerodynamic feedback" allows the wing to operate at higher angles of attack, preventing a sharp decrease in lift as the angle of attack is increased. At large angles of attack (>20 deg), the flow separation for these models likely originates from the leading edge (because the wings have very thin leading edges), and the angle that the leading edge makes to the flow (for a fixed geometric angle of attack) will increase as the speed (and camber) increase. Thus, it is possible that a leading-edge separation at low speed might be alleviated at higher speed as the effective angle of attack at the leading edge is decreased. In the case of bat flight, which motivates these studies, leading-edge separation has been reported for very low-speed flight [9] but, at higher speeds, the animals are observed to adjust the angle of the leading edge during the wing beat cycle by directing the propatagium (the flap of skin in front of the shoulder, elbow, and wrist) with their thumb [20]. We conjecture that the ability to adjust this leading-edge flap, coupled with the adaptive cambering of a compliant membrane, may both serve to suppress leading-edge separation at higher speeds.

Too much camber in thin, rigid airfoils can result in a *decrease* in the lift curve slope. Null and Shkarayev [28] conducted experiments on the effect of camber on the aerodynamics of cambered rigid wings at low Reynolds numbers ($Re = 5.0$–1.0×10^4) and reported that wings with 12% camber showed a dramatically reduced lift curve slope when compared with wings having 3, 6, and 9% camber. In contrast, we do not observe a reduced lift slope in the present results, despite camber values in excess of 20% with the most compliant model tested ($t = 0.10$ mm). In addition, the more-compliant model, which achieved larger cambers, demonstrated higher values of $C_{L_{\max}}$ in contrast to the *rigid*, cambered wings of Null and Shkarayev, which showed more than a 40% decrease in $C_{L_{\max}}$ for a wing with 12% camber. This difference is probably due to the compliance of the wing, which appears to change the character of the separated vortex structure [29]. However, the increased lift of the more-compliant wing comes with a price. As one would expect, the more cambered wing had a larger drag penalty; subsequently, the lift-to-drag ratio suffered as result. It is notable that the two compliant wings, which reached values of maximum camber of $z_{\max} = 10.5$ and 23.8% ($t = 0.1$ and 0.25 mm, respectively) exhibited relatively similar lift characteristics between $\alpha = 10$ and 20 deg, with the only difference between the two wings being the drag performance.

The ability of the membrane wings to maintain lift at high angles of attack despite very large values in camber, coupled to their more gentle stall characteristics, suggest that these configurations may have significant advantages for vehicles operating in gusty conditions or with highly unsteady flight patterns, which are both characteristics of biological flight.

1. *Hysteresis Effects*

If one looks carefully at the most-compliant-membrane lift and drag data, we notice that the symmetry around $\alpha = 0$ appears to be disturbed. This is not experimental inaccuracy, but rather is due to hysteresis in the membrane deformation. The wing is symmetric, and so it has identical aerodynamic performance at both positive and negative angles of attack. At a 0 angle of attack, the wing, theoretically, has zero camber. However, this is an unstable condition and one that is never observed in practice, because the slightest perturbation will cause the wing to break symmetry and to adopt camber. Figure 8 illustrates this behavior in both the lift and drag coefficients, measured by starting at a large negative angle of attack, increasing through zero and on to large positive angles, and then coming back down again. One sees that the wing maintains camber as the incidence angle crosses through zero. At the angle at which the lift finally reaches zero, the wing "snaps" through and adopts the opposite camber. As one would expect, the rigid wing does not show any such hysteresis.

Although not shown here, both rigid and compliant wings exhibit a similar pattern of hysteresis around the stall point, common for low-Reynolds-number wings. $C_L(\alpha)$ on ascent was observed to lie below $C_L(\alpha)$ on descent. The effect was more pronounced for the compliant wing. We assume that in the poststall state the flow is characterized by leading-edge separation due to the bursting of a leading-edge vortex. As α decreases from the poststall state, this leading-edge vortex will reform due to turbulent reattachment. For the rigid wing, the stalled state persists to a slightly lower angle on descent. However, in the case of the compliant wing, the ability of the wing to adjust its camber leads to a more subtle transition over the stall region. However, the details of this flow need to be explored more fully with detailed measurements.

2. *Effects of Wing Aspect Ratio*

Figure 9 presents the lift and drag performance of three compliant wings of varying aspect ratios ($AR = 0.92$–1.78). All three wings had the same membrane compliance and very comparable values of prestrain. We see that their overall behavior is similar, exhibiting the rapid rise in C_L at low values of α, followed by a nearly linear increase in C_L until they experience a soft stall at angles of attack between 30 and 50 deg. Consistent with finite wing theory, the wings with higher AR have higher lift slopes, attributable to the diminished influence of the wing tip vortex for the higher AR wings. However, the lower AR wings exhibit better lift performance at larger, poststall values of α, again due to the now beneficial effects of the tip flow, which suppresses the leading-edge separation. This is particularly

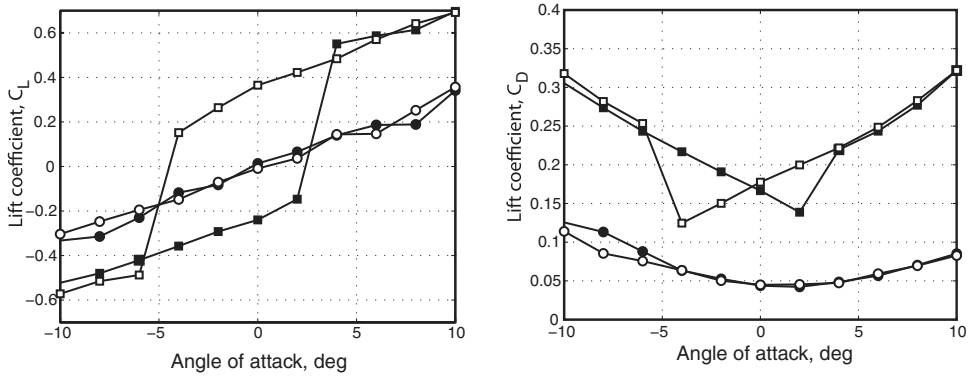

a) Lift performance **b) Drag performance**

Fig. 8 Hysteresis in lift and drag due to compliance. The lift and drag of rigid and compliant wings are compared near a 0 angle of attack. The wings were tested from negative angles, through zero to positive angles, and then back again. Although the C_L and C_D of the rigid wing are independent of the direction of testing, the compliant wing exhibits a significant hysteresis in both C_L and C_D due to the "snap-through" behavior of the membrane as it passes through $\alpha = 0$. ($Re = 1.4 \times 10^5$)

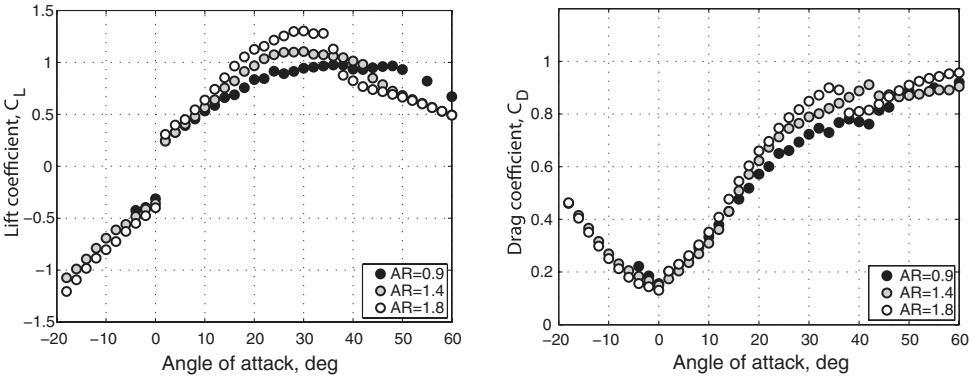

a) Lift performacne **b) Drag performacne**

Fig. 9 Effect of the aspect ratio on the aerodynamic performance. For each of the configurations shown, the membrane prestrain was zero ($\epsilon_0 = 0$), and the membrane thickness ($t = 0.15$ mm) and dynamic pressure per unit span ($\rho U^2 c$) were the same for all the wing configurations. The lift slope decreased with the aspect ratio, exhibiting behavior consistent with finite wing theory of rigid airfoils. For small angles of attack ($\alpha < 15$ deg), the drag behavior was nearly the same for the three aspect ratios. However, for higher angles of attack, the drag increased with the aspect ratio. This may have implications for gliding mammals ($AR \approx 1$) which favor these higher angles of attack in flight.

evident for the $AR = 0.92$ wing, for which C_L reaches a plateau near $\alpha = 20$ deg, which remains almost constant until $\alpha \approx 50$ deg.

The drag coefficients for all three models are nearly identical at low angles of attack ($\alpha < 20$ deg) resulting in increased range efficiency ($C_L = C_D$) for the higher AR wings (not shown here). The drag for the higher AR wings increases more sharply for high angles of attack than the lower AR wings, once again due to the diminished role of the tip vortex flow. The wing with the lowest aspect ratio ($AR = 0.92$) exhibits the best high α range efficiency of all the configurations, an observation that may have implications for mammalian gliders that have aspect ratios very close to 1.0 and thus may be able to achieve higher lift and more efficient performance at the very high angles of attack they tend to favor during flight [7,30].

C. Dynamic Membrane Motions

The compliant membrane wing is unique because of its ability to rapidly adapt in response to changing flow conditions. This also means that the membrane is sensitive to slight variations in the flow about the wing, such as periodic vortex shedding, perturbations in the pressure distribution, etc. We imagine, therefore, that the membrane wing is in constant motion, and in some regimes this motion might be quite substantial. Because the leading edge of the wing is aerodynamically sharp, one assumes that it is sufficient to induce the formation of leading-edge vortices at sufficiently high angles of attack, and one might expect that these shed vortices induce membrane motions. The focus of this section is on characterizing and understanding these membrane motions.

High-speed stereo photogrammetry was used to measure the unsteady motion of the membrane wings. We found that, for every testing condition, some level of membrane vibration was present. By computing the time-averaged root-mean-squared (rms) amplitude of the motion over the entire membrane, a spatial structure for these vibrations was obtained over the full range of operating angles of attack and wind speeds. A typical vibrational mode shape is shown in Fig. 10, in which light and dark regions indicate high and low vibrational amplitudes, respectively. The spatial structures are observed to adopt a standing wave with well-defined nodes and antinodes. These structures resemble the eigenmodes associated with a one-dimensional membrane under tension, subject to Dirichlet boundary conditions at the leading and trailing edges. There are, of course, deviations from the ideal membrane mode shapes, but the analogies are quite apparent. This general eigenmode structure was visible in all cases tested, although the harmonic order of the eigenmode (i.e., the number of peaks in the spatial structure) was found to depend quite strongly on the operating conditions.

We have constructed a phase map of the harmonic order, providing a qualitative picture of the vibrational modes of the membrane (Fig. 11). At lower speeds, the membrane motion is always in the lowest mode, a "breathing" mode in which the entire membrane vibrates in unison. However, higher-order modes and larger amplitude vibrations were excited beyond a critical speed, corresponding to a Reynolds number of approximately 80,000 and in a range of angles of attack falling between 16 and 28 deg. The confinement of the higher eigenvalue modes to this range of Reynolds numbers and angles of attack suggests that the membrane

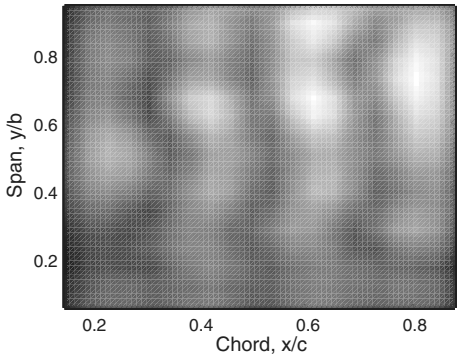

Fig. 10 Spatial pattern of the unsteady vibration of the compliant wing ($\alpha = 28$ deg and $Re = 1.2 \times 10^5$). The membrane undergoes unsteady vibrations with a dominant frequency (in this case 110 Hz) and with a spatial structure related to a drumhead mode, characteristic of the driven vibrations of a membrane under tension.

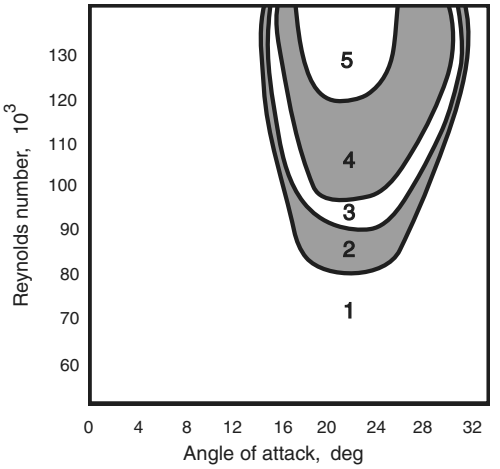

Fig. 11 Phase map of membrane drumhead modes (eigenmodes). The number of modes observed in the membrane spatial vibration is shown as a function of speed and angle of attack, with a region close to stall exhibiting the most complex dependencies, presumably due to active vortex shedding from the leading edge.

is responding to a resonant forcing by the flow at these conditions. In particular, the angles of attack coincide with the onset of stall, when the flow is beginning to separate and one assumes that there is active vortex shedding on the upper wing surface. In contrast to the previous results of Galvao et al. [31], in which the rms magnitudes were nearly uniform in the spanwise direction, the higher magnitudes of the rms values, that is, the stronger vibrations, tended to be near the tip. This difference is believed to be a result of the more than 50% increase in the aspect ratio compared with the wing tested by Galvao, resulting in a decrease in the proportion of the wing influenced by the tip vortices. At angles of attack near stall, the tip flutter induced by flow leakage from the lower to upper surface may be an additional source of vibrational forcing, whereas the leading-edge vortex shedding may act to dampen these vibrations, resulting in the lower rms magnitudes in the inboard region.

To gain some insight into the interaction between the flow structures and the natural frequencies of the membrane, we can model the wing as a planar membrane governed by the wave equation:

$$a\nabla^2 z = \frac{\partial^2 z}{\partial t^2} \tag{14}$$

where a is the membrane wave speed. Because the membrane tip and root are unconstrained, the chordwise tension is much greater than the spanwise tension, allowing us to consider only one-dimensional solutions, $z(x)$. The most energetic vibrational response of the system occurs when it is driven at a frequency close to the membrane's natural frequency, f_0, and harmonics, $f_i = if_0$. Following classical membrane theory [32], the natural frequency, f_0, is dependent on the wave speed, a:

$$f_0 = a/2c \tag{15}$$

which in turn is proportional to the square root of the membrane tension, T:

$$a^2 = T/\rho = (T_o + \epsilon EA)/\rho_m \tag{16}$$

where ρ_m is the mass per unit chordwise length of a membrane with cross-sectional area A. We can estimate these natural frequencies by extending our membrane model described earlier. Assuming once again a parabolic membrane deflection, Eqs. (2–5) can be used to show that the membrane tension varies linearly with the Weber number:

$$T = WeEt/8\rho_m z_{\max} \tag{17}$$

and that the nondimensional frequency, k_0, is related to the Weber number and camber by

$$k_0 = \frac{f_0 c}{U} \sim \frac{1}{U}\sqrt{\frac{We}{z_{\max}}} \tag{18}$$

We have already observed (Fig. 5) that the camber, $z_{\max}$, increases at some rate that is slower than the linear growth, $z_{\max} \sim We^{\eta}$, $(\eta < 1)$, in which case we can predict that the natural frequency of the membrane should decrease with increasing Weber number:

$$k_0 \sim \frac{1}{U}\sqrt{\frac{We}{z_{\max}}} \sim \frac{1}{U}\sqrt{\frac{We}{We^{\eta}}} \sim U^{-\eta/2} \tag{19}$$

This behavior is confirmed by our measurements, shown in Fig. 12. Here we show the frequency spectra of the membrane motion as a function of the Weber number (for a fixed angle of attack, $\alpha = 24$ deg). The spectra were computed from the chord-normal displacement of the membrane, sampled at the point of maximum vibrational amplitude, and are plotted such that the dark shades represent frequencies with high vibrational energy. The solid lines are the predicted membrane frequencies, computed using the measured camber, $z_{\max}$, and Eq. (19).

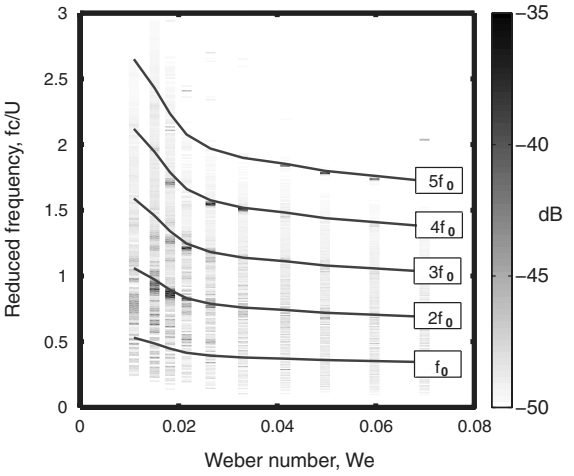

Fig. 12 Unsteady membrane vibrations: waterfall chart illustrating the membrane vibration response as a function of wind speed at a fixed angle of attack ($\alpha = 24$ deg). For each value of the Weber number, the ensemble-averaged power spectral density is estimated from the Fourier transformation of the unsteady time signal of the individual membrane markers. The power densities are plotted as an intensity map, with the higher power densities denoted by darker regions. The frequency is normalized by the freestream velocity and chord, $k_0 = fc/U$. These power spectra are plotted vs the Weber number, defined as $We = \frac{1}{2}\rho U^2 c C_L/(Et)$. Superposed on the spectra are lines of the natural frequency, f_0, and the higher harmonics (integral multiples of f_0) of the membrane predicted using membrane theory in which $f_0 = \sqrt{T/\rho_m}/(2c)$, where T and ρ are the membrane tension and the mass per unit chord length, respectively. The tension is estimated from the observed camber of the wing at each point tested.

At low Weber numbers, the membrane tends to be excited at the second eigenmode, $2f_0$, corresponding to a Strouhal number of approximately 0.8. This selection mechanism might be due to a resonance between the natural frequencies of the membrane and of vortex shedding from the leading edge. As each vortex is released, it imparts a pressure pulse on the upper surface of the membrane and, if the shedding and vibrational frequencies are close, one would expect the membrane to respond as a forced oscillator. However, as the Weber number increases (i.e., the velocity increases), we see an interesting and unexpected result: the dominant response of the membrane jumps (in an almost quantized manner) to higher and higher frequencies, each time closely matching the frequency predicted by our analysis but associated with higher membrane eigenmodes. The spatial response of the membrane at each speed (Fig. 11) closely matches this trend.

The reason for this migration to higher frequencies remains somewhat of a puzzle. We see two possible explanations. The first is that the forcing frequency due to vortex shedding (from the leading edge or the laminar separation bubble) remains constant. As the nondimensional natural frequency of the membrane falls, as predicted by the theory, the membrane responds to the forcing through some nonlinear resonance mechanism such that the membrane response is at the closest integer multiple of the forcing frequency present in the flow. Although this explanation may be valid, a second (more plausible) possibility is that the forcing frequency also increases with speed (or Weber number). In many flows, one expects that the Strouhal number for the vortex shedding from a bluff body is nearly constant over a large range of Reynolds (or Weber) numbers. However, this result is only strictly valid for high-Reynolds-number flows, and recent experiments by Yerusevych et al. [33] of symmetric airfoil wakes have shown that the Strouhal number of the wake vortex shedding can increase significantly at low Reynolds numbers, attributable to the presence of a separation bubble that can exert a significant influence on the subsequent shear layer instabilities. This effect could well be occurring in the present case, but without the benefit of supporting velocity field measurements, it is impossible to fully explain these observations.

V. Conclusions

The results obtained in this series of experiments include some subtleties that are quite diverse, and there are several features of the flow over compliant wings that are quite surprising and unexpected. As compared with a rigid wing, the compliant membrane wings generate more lift with higher lift slopes because the camber of the wing increases dynamically with increasing aerodynamic loading. In addition, the most-compliant-membrane model also exhibits a less-severe decrease in lift at the onset of stall than the rigid and less-compliant wing due to the decambering of the wing as the flow starts to separate. Lastly, stall is observed to be delayed in the compliant wings by as much as 10 deg. As has been pointed out before [22], to understand the effects of compliance, a key nondimensional parameter must be added to the description of the flow. The Weber number effectively describes the interaction between the aerodynamic loading (either by dynamic pressure or angle of incidence) and the membrane elasticity, and this must be considered when performing scale tests or making comparisons with animal flight. Although the compliant membrane wings have the advantage of increased lift, they also exhibit increased drag, although the overall effect on lift to drag is still generally improved. Indeed, the membranes that had been prestrained ($\epsilon_0 > 0$) exhibited better aerodynamic efficiencies than the model with no prestrain. Despite these complexities, two simple analytical models predicted the static and dynamic deformations with surprising accuracy. These models can certainly be improved. In particular, the static model would benefit from the use of a higher-order model (for example, incorporating thin-airfoil and lifting-line theory) to predict the aerodynamic loading as a function of the angle of incidence and aspect ratio. The dynamic model does a good job of predicting the membrane frequencies, but still needs a means to predict the frequency of fluid forcing due to leading-edge vortex shedding.

Bat flight, like most animal flight, is characterized by low-Reynolds-number flight regimes, and we expect that the effects of the Reynolds number will be critical to understanding the aerodynamic behavior of these membrane wings. Clearly, the details of the transition to turbulence, the factors that influence leading-edge separation and turbulent reattachment, are strongly influenced by the low-Reynolds-number flight environment, although a detailed study of these issues was not the focus of this study. However, for these experiments, which were conducted at a variety of wind speeds using a model of fixed dimension, we varied both the Reynolds and Weber numbers by changing the freestream velocity; thus, it can be difficult to tease these effects apart. However, over the narrow range of speeds tested, the primary effects observed are clearly due to *Weber* number effects, rather than *Reynolds* number effects. This assertion is supported by the generally excellent collapse of the wing camber data (Fig. 5) over the range of We tested. Having said this, low-Reynolds-number effects are clearly critical and deserve close attention in future experiments.

The motivation for this study originated in a desire to better understand the fundamentals of the aerodynamics of gliding mammals, such as flying squirrels or sugar gliders. Recent studies of the mechanics of live mammalian gliders by Bishop [30] provide an opportunity to evaluate the extent to which these physical models capture important features observed in gliding mammals. In those experiments, flying squirrels were observed to glide at average angles of attack of $\alpha = 42.5$ deg, whereas sugar gliders averaged $\alpha = 44.2$ deg. At these angles of attack, the flying squirrels and sugar gliders produced lift coefficients averaging 2.12 and 1.48, respectively, with drag coefficients averaging 0.98 and 1.08. This corresponds to range efficiencies (C_L/C_D) of 2.26 and 1.39 for the squirrels and sugar gliders, respectively. The lowest-aspect-ratio model in the present study ($AR = 0.92$) has the most similar geometry to these species and, at similar angles of attack, the physical models demonstrated a lift coefficient of 0.95 and a drag coefficient of 0.81 for a range efficiency of 1.17. In Bishop's study, the sugar gliders exhibited aerodynamic performance similar to this $AR = 0.92$ compliant-membrane wing. In contrast, the flying squirrels appear to generate substantially more lift with only a slight increase in drag. Flying squirrels have morphological specializations that allow the use of the thumb to control the angle of the leading edge of the wing. Sugar gliders do not have this morphological feature, and their wings more closely resemble the simplified physical models tested in this study. We propose that this anatomical feature may be operated in a manner similar to a leading-edge flap on human-engineered vehicles. This articulated leading-edge flap allows the flying squirrels to maintain attached flow and, consequently, to achieve high values of C_L at high incidence angles. It should be noted that bats also possess this articulated leading-edge flap feature.

Mammalian gliders typically glide at relatively high values of the glide angle, that is, the angle of descent with respect to the horizontal. In addition, these animals glide at high angles of attack that in combination with large values of glide angle put the animals' body angles near horizontal, that is, perpendicular to gravity. In this flight configuration, the lift will contribute to the animals' thrust in addition to counteracting gravity. Similarly, at these angles, the drag force contributes to weight support. Therefore, increased drag due to the higher camber of the compliant wings is not as undesirable as one might first think. In the experiments presented in this paper, the highest lift-to-drag ratio was observed for models for which the camber remains relatively small (below 14% of the chord). Similarly, Bishop [30] found that the wing camber of flying squirrels and sugar gliders averaged 10% of their chord length, with the camber exceeding 14% in only a few of the flights of the flying squirrels.

Finally, the compliant wings permit relatively efficient flight for a wide range of extreme angles of attack ($\alpha > 30$). This kind of aerodynamic performance would be desirable in natural flight as well as for micro air vehicles, for which such aerodynamic performance is necessary to ensure robust flight characteristics over a wide range of flight conditions, including gusts and variations due to sudden maneuvers to avoid obstacles and other hazards. These experiments represent a small window into the subtle and complex performance of flexible aerodynamic structures and, certainly, much more needs to be investigated.

Acknowledgments

This work was supported by the Air Force Office of Scientific Research (monitored by Rhett Jeffries and Willard Larkin), the National Science Foundation, and the Brown University Undergraduate Teaching and Research Award program. We gratefully acknowledge the members of our research lab at Brown, whose assistance has been invaluable. Special thanks to Brian Corkum, who helped fabricate the model apparatus. An early version of this paper was presented at the 2008 AIAA Aerospace Sciences Meeting in Reno NV, at which time we became aware of two papers, one by Rojratsirikul et al. (Rojratsirikul, P., Wang, Z., and Gursul, I., "Unsteady Aerodynamics of Membrane Airfoils," AIAA Paper 2008-613, Jan. 2008.) and one by Gordnier (Gordnier, R. E., "High Fidelity Computational Simulation of a Membrane Wing Airfoil," AIAA Paper 2008-614, Jan. 2008.), concerning the behavior of two-dimensional membrane wings, with findings closely related to the present work.

References

[1] Ellington, C. P., "The Aerodynamics of Hovering Insect Flight. Parts 1-6," *Philosophical Transactions of the Royal Society of London. Series B, Biological Sciences*, Vol. 305, No. 1122, Feb. 1984, pp. 1–181. doi:10.1098/rstb.1984.0049

[2] Sane, S. P., and Dickinson, M. H., "The Aerodynamic Effects of Wing Rotation and a Revised Quasi-Steady Model of Flapping Flight," *The Journal of Experimental Biology*, Vol. 205, No. 8, 2002, pp. 1087–1096.

[3] Lehmann, F., Sane, S., and Dickinson, M., "The Aerodynamic Effects of Wing–Wing Interaction in Flapping Insect Wings," *The Journal of Experimental Biology*, Vol. 208, No. 16, 2005, pp. 3075–3092. doi:10.1242/jeb.01744

[4] Swartz, S. M., Bishop, K. L., and Ismael-Aguirre, M.-F., "Dynamic Complexity of Wing Form in Bats: Implications for Flight Performance," *Functional and Evolutionary Ecology of Bats*, edited

by Z. Akbar, G. McCracken, and T. H. Kunz, Oxford Univ. Press, Oxford, England, U.K., 2005.

[5] Tian, X., Iriarte-Diaz, J., Middleton, K., Galvao, R., Israeli, E., Roemer, A., Sullivan, A., Song, A., Swartz, S., and Breuer, K., "Direct Measurements of the Kinematics and Dynamics of Bat Flight," *Bioinspiration & Biomimetics*, Vol. 1, Dec. 2006, pp. S10–S18. doi:10.1088/1748-3182/1/4/S02

[6] Riskin, D., Willis, D., Iriarte-Diaz, J., Hedrick, T., Kostandov, M., Chen, J., Laidlaw, D., Breuer, K., and Swartz, S., "Describing Bat Wing Kinematics Accurately: Quantifying Complexity with Proper Orthogonal Decomposition," *The Journal of Theoretical Biology* (submitted for publication).

[7] Bishop, K., "The Relationship Between 3-D Kinematics and Gliding Performance in the Southern Flying Squirrel, *Glaucomys volans*," *The Journal of Experimental Biology*, Vol. 209, No. 4, 2006, pp. 689–701. doi:10.1242/jeb.02062

[8] Hedenstrom, A., Johansson, L., Wolf, M., von Busse, R., Winter, Y., and Spedding, G., "Bat Flight Generates Complex Aerodynamic Tracks," *Science*, Vol. 316, No. 5826, May 2007, pp. 894–897. doi:10.1126/science.1142281

[9] Muijres, F. T., Johansson, L. C., Bareld, R., Wolf, M., Spedding, G. R., and Hedenstrom, A., "Leading-Edge Vortex Improves Lift in Slow-Flying Bats," *Science*, Vol. 319, No. 5867, 2008, pp. 1250–1253. doi:10.1126/science.1153019

[10] Lian, Y., and Shyy, W., "Laminar-Turbulent Transition of a Low Reynolds Number Rigid or Flexible Airfoil," *AIAA Journal*, Vol. 45, No. 7, 2007, pp. 1501–1513. doi:10.2514/1.25812

[11] Lissaman, P., "Low-Reynolds-Number Airfoils," *Annual Review of Fluid Mechanics*, Vol. 15, Jan. 1983, pp. 223–239. doi:10.1146/annurev.fl.15.010183.001255

[12] Shyy, W., Klevebring, F., Nilsson, M., Sloan, J., Carroll, B., and Fuentes, C., "Rigid and Flexible Low Reynolds Number Airfoils," *Journal of Aircraft*, Vol. 36, No. 3, 1999, pp. 523–529.

[13] Pelletier, A., and Mueller, T., "Low Reynolds Number Aerodynamics of Low-Aspect-Ratio Thin/Flat/Cambered-Plate Wings," *AIAA Journal*, Vol. 37, No. 5, 2000, pp. 825–832.

[14] Torres, G., and Mueller, T., "Low-Aspect-Ratio Wing Aerodynamics at Low Reynolds Numbers," *AIAA Journal*, Vol. 42, No. 5, 2004, pp. 865–873. doi:10.2514/1.439

[15] Nielsen, J., "Theory of Flexible Aerodynamic Surfaces," *Journal of Applied Mechanics*, Vol. 30, Sept. 1963, pp. 435–442.

[16] Thwaites, B., "The Aerodynamic Theory of Sails 1: Two-Dimensional Sails," *Proceedings of the Royal Society A: Mathematical, Physical and Engineering Sciences*, Vol. 261, No. 1306, May 1961, pp. 402–422. doi:10.1098/rspa.1961.0086

[17] Jackson, P., "A Simple Model for Elastic Two-Dimensional Sails," *AIAA Journal*, Vol. 21, No. 1, 1983, pp. 153–155. doi:10.2514/3.60106

[18] Lorillu, O., Weber, R., and Hureau, J., "Numerical and Experimental Analysis of Two-Dimensional Separated Flows over a Flexible Sail," *Journal of Fluid Mechanics*, Vol. 466, Sept. 2002, pp. 319–341. doi:10.1017/S0022112002001283

[19] Newman, B., and Low, H., "Two-Dimensional Impervious Sails: Experimental Results Compared with Theory," *Journal of Fluid Mechanics*, Vol. 144, July 1984, pp. 445–462. doi:10.1017/S0022112084001683

[20] Song, A., Riskin, D., Swartz, S., and Breuer, K. S., "Bat Wing Membrane Extension and Orientation During Flight," 2008 (unpublished).

[21] Shyy, W., Berg, M., and Ljungqvist, D., "Flapping and Flexible Wings for Biological and Micro Air Vehicles," *Progress in Aerospace Sciences*, Vol. 35, No. 5, 1999, pp. 455–505. doi:10.1016/S0376-0421(98)00016-5

[22] Shyy, W., Ifju, P., and Viieru, D., "Membrane Wing-Based Micro Air Vehicles," *Applied Mechanics Reviews*, Vol. 58, No. 4, July 2005, pp. 283–301. doi:10.1115/1.1946067

[23] Lian, Y. S., Shyy, W., Viieru, D., and Zhang, B. N., "Membrane Wing Aerodynamics for Micro Air Vehicles," *Progress in Aerospace Sciences*, Vol. 39, Nos. 6–7, 2003, pp. 425–465. doi:10.1016/S0376-0421(03)00076-9

[24] Stanford, B., Sytsma, M., Albertani, R., Viieru, D., Shyy, W., and Ifju, P., "Static Aeroelastic Model Validation of Membrane Micro Air Vehicle Wings," *AIAA Journal*, Vol. 45, No. 12, 2007, pp. 2828–2837. doi:10.2514/1.30003

[25] Swartz, S., Groves, M., Kim, H., and Walsh, W., "Mechanical Properties of Bat Wing Membrane Skin," *Journal of Zoology: Proceedings of the Zoological Society of London*, Vol. 239, No. 2, 1996, pp. 357–378.

[26] Mikhail, E., Bethel, J., and McGlone, J., *Introduction to Modern Photogrammetry*, Wiley, New York, 2001.

[27] Torres, G., and Mueller, T., "Aerodynamic Characteristics of Low Aspect Ratio Wings at Low Reynolds Numbers," *Fixed and Flapping Wing Aerodynamics for Micro Air Vehicle Applications*, edited by T. Mueller, AIAA, Reston, VA, 2001, Chap. 7, pp. 115–141.

[28] Null, W., and Shkarayev, S., "Effect of Camber on the Aerodynamics of Adaptive-Wing Micro Air Vehicles," *Journal of Aircraft*, Vol. 42, No. 6, 2005, pp. 1537–1542. doi:10.2514/1.12401

[29] Gordnier, R. E., "High Fidelity Computational Simulation of a Membrane Wing Airfoil," AIAA Paper 2008-614, Jan. 2008.

[30] Bishop, K., "Aerodynamic Force Generation, Performance and Control of Body Orientation During Gliding in Sugar Gliders (*Petaurus breviceps*)," *The Journal of Experimental Biology*, Vol. 210, No. 15, 2007, pp. 2593–2606. doi:10.1242/jeb.002071

[31] Galvao, R., Israeli, E., Song, A., Tian, X., Bishop, K., Swartz, S., and Breuer, K., "The Aerodynamics of Compliant Membrane Wings Modelled on Mammalian Flight Mechanics," AIAA Paper 2006-2866, June 2006.

[32] Rayleigh, J. W. S., *The Theory of Sound*, 2nd ed., Macmillan, London, 1894.

[33] Yarusevych, S., Sullivan, P., and Kawall, J., "Coherent Structures in an Airfoil Boundary Layer and Wake at Low Reynolds Numbers," *Physics of Fluids*, Vol. 18, No. 4, 2006, pp. 044101–044101-11. doi:10.1063/1.2187069

E. Livne
Associate Editor